J Mater Sci: Mater Electron (2017) 28:543–552
DOI 10.1007/s10854-016-5557-3

Bi_2MoO_6/RGO composite nanofibers: facile electrospinning fabrication, structure, and significantly improved photocatalytic water splitting activity

Jing Zhao[1] · Ying Yang[1] · Wensheng Yu[1] · Qianli Ma[1] · Xiangting Dong[1] · Xinlu Wang[1] · Jinxian Wang[1] · Guixia Liu[1]

Received: 12 June 2016 / Accepted: 12 August 2016 / Published online: 20 August 2016

Abstract Bi_2MoO_6/reduced graphene oxide (RGO) composite nanofibers were successfully fabricated by calcining the electrospun polyvinyl pyrrolidone (PVP)/RGO/$[(NH_4)_6Mo_7O_{24} + Bi(NO_3)_3]$ composite nanofibers. The products were investigated in detail by X-ray diffractometer, scanning electron microscope, transmission electron microscope, UV–Vis diffuse reflectance spectroscope and X-ray photoelectron spectroscope. The as-prepared Bi_2MoO_6/RGO composite nanofibers are pure orthorhombic phase with space group of Pbca, and the diameter is 132 ± 18 nm. These nanocomposite samples display high photocatalytic hydrogen production activity in aqueous solutions containing methanol as sacrificial reagent under visible light irradiation. Bi_2MoO_6/5 % RGO composite nanofibers used as photocatalyst for water splitting exhibit the highest H_2 evolution rate of 794.72 μmol h^{-1}, which is improved by 2.86 times compared to Bi_2MoO_6 nanofibers. The enhancement of photocatalytic hydrogen production performance is due to addition of RGO, the intimate interfacial contact and large contact area between Bi_2MoO_6 nanoparticles and RGO sheets, which help to make full use of the electron conductivity of RGO for transferring the photogenerated electrons and separating the photoproduced carriers. Therefore the electrospinning is a facile and effective technique to fabricate Bi_2MoO_6/RGO composite nanofibers which could take advantage of solar energy to achieve efficient H_2-evolution from water splitting.

✉ Wensheng Yu
wenshengyu2009@sina.com

✉ Xiangting Dong
dongxiangting888@163.com

[1] Key Laboratory of Applied Chemistry and Nanotechnology at Universities of Jilin Province, Changchun University of Science and Technology, Changchun 130022, China

1 Introduction

To solve the problems of global energy crisis and environmental pollution, a lot of new energy resources have been developed by researchers, such as biofuel, silicon cell, geothermal power, etc. Among them, hydrogen has been considered to be a storable, clean and environmental-friendly fuel of the future, photocatalytic water splitting into hydrogen has been considered as a significant and attractive solution to solve the global energy and environmental problems [1, 2]. Semiconductors have been at the forefront of photocatalytic water splitting for the synthesis of renewable fuels ever since the discovery of TiO_2 in 1972 by Honda and Fujishima [3]. So far, various semiconductor photocatalysts have been investigated, such as SiC [4], TiO_2 [5], Bi_2WO_6 [6], C_3N_4 [7], $La_2Ti_2O_7$ [8], CdS [9], Bi_2MoO_6 [10], etc. Among them, low-temperature phase γ-Bi_2MoO_6 is one of the simplest Aurivillius phase perovskite, which consists of perovskite layers $(MoO_4)^{2-}$ sandwiched between $(Bi_2O_2)^{2+}$ layers [11]. The conduction band (CB) of Bi_2MoO_6 is composed of the Mo 3d orbital, its valence band (VB) is formed by the hybridization of the O 2p and Bi 6s orbitals, which not only makes the VB largely dispersed and thus results in band gap of Bi_2MoO_6 ($\sim$2.7 eV) capable of absorbing visible light ($\lambda > 400$ nm), but also favors the mobility of photogenerated holes for specific oxidation reaction [12]. It has attracted a great deal attention because of its excellent properties such as low toxicity and cost, high stability, and excellent visible-light activity for various practical applications. It has been reported that Bi_2MoO_6 could be

used as photocatalyst for the degradation of organic pollutants and water splitting under visible-light irradiation owing to its high efficiency [13, 14]. Several methods have well been developed to fabricate Bi_2MoO_6, such as aerosol-spraying [15], electrospinning [16], hydrothermal treatment [17], template method [18] and co-precipitation [19].

However, a major limitation to achieve higher photocatalytic efficiency is the rapid recombination of photogenerated electrons and holes. The kinetics of recombination is faster than that of surface redox reactions, which greatly reduces the photocatalytic efficiency of photocatalyst [20]. Therefore, how to design and fabricate more highly efficient Bi_2MoO_6-based photocatalysts remains a huge challenge. In recent years, Bi_2MoO_6 doped with suitable materials has been attempted to improve the photocatalytic performances of Bi_2MoO_6 composites [21, 22]. Reduced graphene oxide (denoted as RGO for short), as a single layer of graphite, has received extensive attention recently due to its unique two-dimensional structure, extraordinary electronic properties and electron transport capabilities, superior electron mobility and extremely high specific surface area [23]. These unique properties suggest that graphene has great potential for providing new approaches and critical improvements in the field of electrochemistry. In particular, graphene-based semiconductor photocatalysts have attracted extensive attention because of their promising usage in environmental and energy applications [24]. Recently, a large number of fabrication methods have already been employed to fabricate Bi_2MoO_6/RGO nanomaterials and their photocatalytic activity were also investigated. Zhang et al. [25] reported a hydrothermal method to fabricate Bi_2MoO_6/RGO composite nanoplates, which showed remarkable enhancement in the visible light driven photocatalytic destruction of bacteria when compared to pure Bi_2MoO_6. A simple one-step process was developed for preparation of Bi_2MoO_6/RGO composites by Wang, and the Bi_2MoO_6/RGO composites showed an increase in photocatalytic activity compared with pure Bi_2MoO_6 under visible light irradiation [26]. In order to obtain a new morphological nanostructure of Bi_2MoO_6/RGO composites with high efficient photocatalysis, fabrication of Bi_2MoO_6/RGO composite nanofibers is a meaningful subject of study. To our knowledge, there are few reports on the preparation of Bi_2MoO_6/RGO composite nanofibers by using electrospinning technique and their photocatalytic water splitting in references.

Electrospinning is a simple, convenient, straightforward and versatile technique for preparing long fibers with diameters ranging from tens of nanometers up to micrometer [27, 28]. This method not only attracts extensive academic investigation, but is also applied in many areas in the previous reports [29, 30]. The one-dimensional nanofibers constructed by electrospinning technique have a better capability of electron transportation and intimate interfacial contact area between semiconductor and RGO in the nanocomposites, both of them could improve the photocatalytic performance of photocatalyst. These benefits of electrospinning to prepare one-dimensional Bi_2MoO_6/RGO composite nanofibers used for photocatalytic water splitting can be fully utilized. In this work, Bi_2MoO_6/RGO composite nanofibers were prepared by calcining the electrospun PVP/RGO/[$(NH_4)_6Mo_7O_{24}$ + $Bi(NO_3)_3$] composite nanofibers. The samples were systematically characterized by using modern measurements techniques, and the photocatalytic water splitting activity and possible mechanism of Bi_2MoO_6/RGO composite nanofibers were also studied, and some new and significant results were obtained.

2 Experimental sections

2.1 Materials

Polyvinyl pyrrolidone (PVP K90, $M_w = 90{,}000$) was bought from Tiantai Chemical Co., Ltd. Natural graphite was purchased from Qingdao Chenyang graphite, Ltd. Bismuth nitrate pentahydrate [$Bi(NO_3)_3{\cdot}5H_2O$] and phosphorus(V) oxide (P_2O_5) were purchased from Xilong Chemical Co., Ltd. *N,N*-dimethylformamide (DMF) and ammonium tungstate [$(NH_4)_6Mo_7O_{24}$] were bought from Sinopharm Chemical Reagent Co., Ltd. Citric acid ($C_6H_8O_7$) and potassium persulfate ($K_2S_2O_8$) were purchased from Beijing chemical works. Methanol (CH_3OH) was bought from Kemiou Chemical Co. Ltd. All chemicals were of anticalyal reagent grade and directly used as received without further purification. Deionized water was homemade in our lab.

2.2 Preparation of Bi_2MoO_6/RGO composite nanofibers via electrospinning

RGO was synthesized from natural graphite by a modified Hummers method, as described in the Ref. [31, 32]. In the typical procedure of preparing Bi_2MoO_6/5 % RGO composite nanofibers, 0.2472 g of $(NH_4)_6Mo_7O_{24}$ and 0.5884 g of citric acid were dissolved in deionized water at elevated temperature to form a mixture of $(NH_4)_6Mo_7O_{24}$ and citric acid, and the mixture was dissolved in 12.8436 g of DMF to form transparent solution. The RGO was added into the above solution, and the color of the suspension turned black. Then the suspension was sonicated at ambient temperature for 1 h using a high-intensity ultrasonic cleaner (40 kHz, 100 W). Next, 1.3583 g of $Bi(NO_3)_3{\cdot}5H_2O$

and 1.6055 g of PVP were added into the above suspension and the mixture was magnetically stirred for 8 h to form a homogeneous spinning solution. Subsequently, the spinning solution was electrospun at room temperature under a positive high voltage of 13 kV, the distance between the spinneret tip and the collector (aluminum foil) was fixed to 15 cm, and the angle between the spinneret and horizontal plane was set to 30°, and the atmosphere relative humidity was 30–60 %. With the volatilization of DMF and water, PVP/RGO/[$(NH_4)_6Mo_7O_{24}$ + $Bi(NO_3)_3$] composite nanofibers were acquired on the collector. After the composite nanofibers were calcined at 450 °C for 2 h in air with a heating rate of 1 °C·min^{-1}, followed by natural cooling down to room temperature, Bi_2MoO_6/5 % RGO composite nanofibers were successfully obtained. Other series of Bi_2MoO_6/*x*RGO (x = 2, 5, 8 %, x stands for mass ratio of RGO to Bi_2MoO_6) composite nanofibers were prepared by the similar procedure except for adding different masses of RGO.

2.3 Synthesis of Bi_2MoO_6 nanofibers

For comparison, Bi_2MoO_6 nanofibers were also prepared via electrospinning under the same conditions only without adding RGO. In order to investigate the influence of the interfacial interaction between RGO and Bi_2MoO_6 nanofibers on the hydrogen yield, the sample was prepared by mechanical mixing RGO with Bi_2MoO_6 nanofibers and labelled as Bi_2MoO_6 + 5 % RGO.

2.4 Hydrogen production measurements

Photocatalytic hydrogen evolution tests were carried out in a Labsolar-IIIAG photocatalytic system device (Beijing Bofeilai Technology Co., Ltd) with external light irradiation. The light source was a Xenon lamp (300 W, PLS-SXE300/300UV, China) equipped with cutoff filter L38 ($380 < \lambda < 750$ nm). Prior to testing, 0.1 g of the photocatalyst (Bi_2MoO_6, Bi_2MoO_6/xRGO, Bi_2MoO_6 + 5 % RGO), 25 mL of methyl alcohol and 75 mL tap water were added into a 200-mL quartz cuvette successively under vigorous magnetic stirring to ensure the sample was suspended similarly. Then the suspension was degassed by evacuation. All of the experiments were conducted at room temperature. The amount of gas produced was determined using gas chromatography (GC7900, Tianmei Techcomp Ltd., thermal conductivity detector, nitrogen used as carrier gas).

2.5 Characterization methods

X-ray diffraction (XRD) measurement was performed using a Rigaku D/max-RA XRD diffractometer with Cu Kα line of 0.15418 nm. The field emission scanning electron microscope (FESEM, XL-30 FEI Company) was used to characterize the morphologies and sizes of the products. The compositions of samples were examined by OXFORD ISIS-300 energy dispersive X-ray spectrometer (EDX). Transmission electron microscope (TEM) analysis was carried out using a JEM-2010 TEM under a working voltage of 200 kV. The histograms of diameters were drawn by Image-Pro Plus 6.0 and origin 8.5 software. UV–Vis diffuse reflectance spectra of the samples were obtained on a UV–Vis spectrophotometer (Hitachi U-3010) using $BaSO_4$ as the reference. X-ray photoelectron spectra (XPS) of the samples were recorded on an ESCALAB 250Xi instrument (ESCALAB 250Xi, America), with monochromatized Al Kα radiation (1486.6 eV) at 14 kV and 20 mA, and a pressure lower than 10^{-9} mbar.

3 Results and discussion

3.1 Crystal structure

The phase structures of Bi_2MoO_6, Bi_2MoO_6/*x*RGO and Bi_2MoO_6 + 5 % RGO were characterized by XRD, and the results are shown in Fig. 1. The characteristic diffraction peaks [2θ = 28.3°(131), 32.6°(002), 33.2°(060), 36.2°(151), 46.8°(202), 47.2°(062), 55.6°(133), 56.3°(280), 58.5°(262), 66.1°(193), 67.7°(412), etc.] of the samples can be easily indexed to the orthorhombic phase of Bi_2MoO_6 (PDF card no. 72-1524). It is also found that the main diffraction peaks of Bi_2MoO_6/xRGO are similar to those of Bi_2MoO_6. No characteristic diffraction peaks of RGO are detected in the all Bi_2MoO_6/xRGO composites. This can be ascribed to the fact that the content of RGO is low and it is uniformly dispersed in Bi_2MoO_6, thereby the RGO could not be identified by XRD. This result is in accordance with that reported by group of Wang [26].

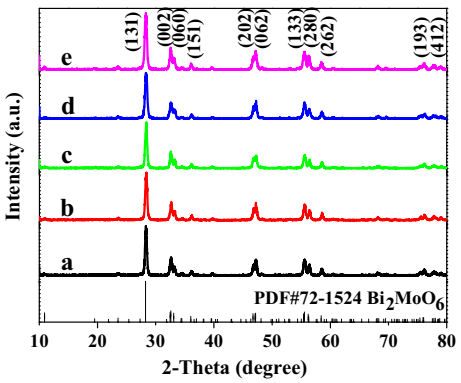

Fig. 1 XRD patterns of Bi_2MoO_6 (**a**), Bi_2MoO_6/2 % RGO (**b**), Bi_2MoO_6/5 % RGO (**c**), Bi_2MoO_6/8 % RGO (**d**) and Bi_2MoO_6 + 5 % RGO (**e**) composite nanofibers with PDF standard card of Bi_2MoO_6

3.2 Morphology and element analysis

The morphologies of the as-prepared PVP/[$(NH_4)_6Mo_7O_{24}$ + $Bi(NO_3)_3$] and PVP/RGO/[$(NH_4)_6Mo_7O_{24}$ + $Bi(NO_3)_3$] composite nanofibers were observed by means of SEM, as presented in Fig. 2a, c, respectively. From the images one can see that the as-prepared PVP/[$(NH_4)_6Mo_7O_{24}$ + $Bi(NO_3)_3$] and PVP/RGO/[$(NH_4)_6Mo_7O_{24}$ + $Bi(NO_3)_3$] composite nanofibers are relatively smooth. The average diameter of the PVP/[$(NH_4)_6Mo_7O_{24}$ + $Bi(NO_3)_3$] and PVP/RGO/[$(NH_4)_6Mo_7O_{24}$ + $Bi(NO_3)_3$] composite nanofibers are 250 ± 24 and 274 ± 35 nm under the confidence level of 95 %, as respectively shown in Fig. 2b,d. Figure 3a, c demonstrate FESEM images of Bi_2MoO_6 and Bi_2MoO_6/5 % RGO composite nanofibers, respectively. It can be clearly seen that the morphologies of Bi_2MoO_6 and Bi_2MoO_6/5 % RGO are nanofibrous structure. After calcinated at 450 °C in the air, the surfaces of Bi_2MoO_6 and Bi_2MoO_6/5 % RGO composite nanofibers are respectively coarser than those of PVP/[$(NH_4)_6Mo_7O_{24}$ + $Bi(NO_3)_3$] and PVP/RGO/[$(NH_4)_6Mo_7O_{24}$ + $Bi(NO_3)_3$] composite nanofibers. As seen from Fig. 3b, d, the average diameters of the Bi_2MoO_6 and Bi_2MoO_6/5 % RGO are respectively 124 ± 20 and 132 ± 18 nm under the confidence level of 95 %.

EDX spectra of PVP/[$(NH_4)_6Mo_7O_{24}$ + $Bi(NO_3)_3$], PVP/RGO/[$(NH_4)_6Mo_7O_{24}$ + $Bi(NO_3)_3$], Bi_2MoO_6 and Bi_2MoO_6/5 % RGO composite nanofibers are manifested in Fig. 4. The presence of Bi, Mo, O elements corresponds to Bi_2MoO_6. Pt peak is from the conductive film of Pt plated on the sample for SEM observation. As revealed in Fig. 4c, d, after calcinated at 450 °C in the air, only a few carbon is detected by EDX analysis, indicating the removal of the PVP template. The presence of C element in Bi_2MoO_6 is due to the residual traces from the organics, and C element in Bi_2MoO_6/5 % RGO results from RGO and residual traces from the organics. No other impurity elements are found, implying that the as-prepared nanofibers are pure.

The TEM image of Bi_2MoO_6/5 % RGO composite nanofibers is presented in Fig. 5a. As seen from Fig. 5a, RGO nanosheets are covered on the Bi_2MoO_6 particles, indicating that Bi_2MoO_6/5 % RGO composite nanofibers are composed of Bi_2MoO_6 nanoparticles with size of 30–50 nm and RGO nanosheets. To better study the interface structure between the two phases, the Bi_2MoO_6/5 % RGO was further examined with high-resolution TEM (HR-TEM), as revealed in Fig. 5b. As seen from Fig. 5b, the well-crystallized structure with lattice spacing of 0.316 nm corresponds to the (1 3 1) plane of the orthorhombic Bi_2MoO_6 [33]. The lattice fringes of RGO exhibit an interplanar spacing of 0.35 nm and it corresponds to (0 0 2) planar facet of RGO [34]. It can be further seen from Fig. 5b that the RGO sheets with the basal plane are perfectly bridged with Bi_2MoO_6. TEM analysis indicates that Bi_2MoO_6/5 % RGO composite nanofibers are successfully prepared.

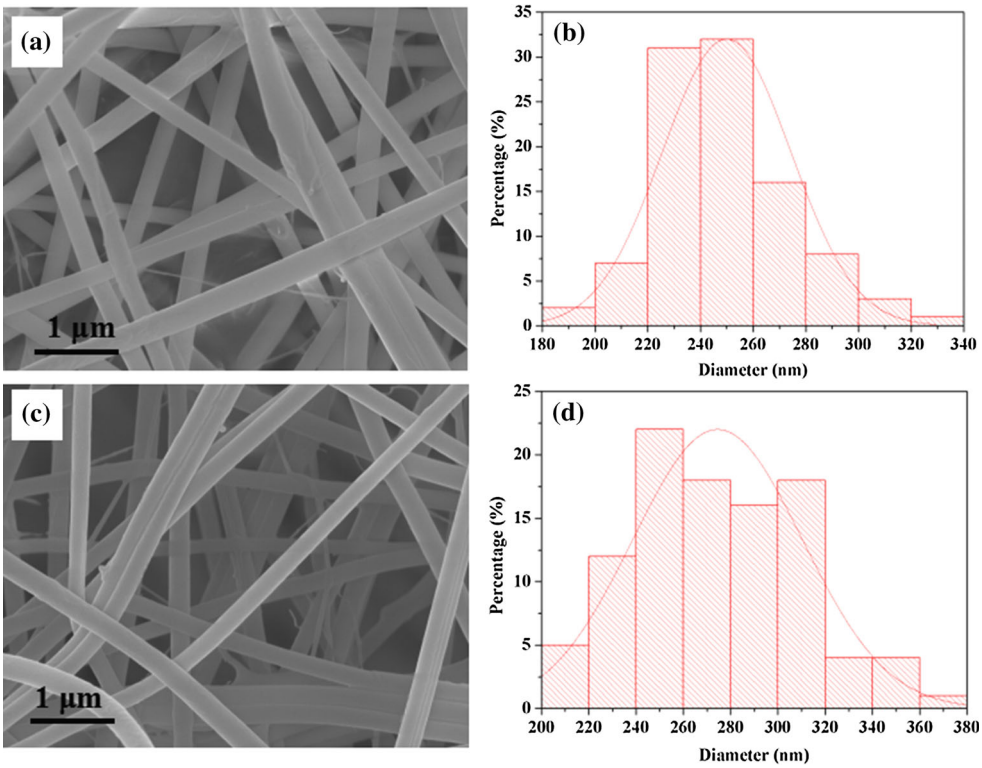

Fig. 2 SEM images (**a**, **c**) and histograms (**b**, **d**) of diameters of PVP/[$(NH_4)_6Mo_7O_{24}$ + $Bi(NO_3)_3$] (**a**, **b**) and PVP/RGO/[$(NH_4)_6Mo_7O_{24}$ + $Bi(NO_3)_3$] (**c**, **d**) composite nanofibers

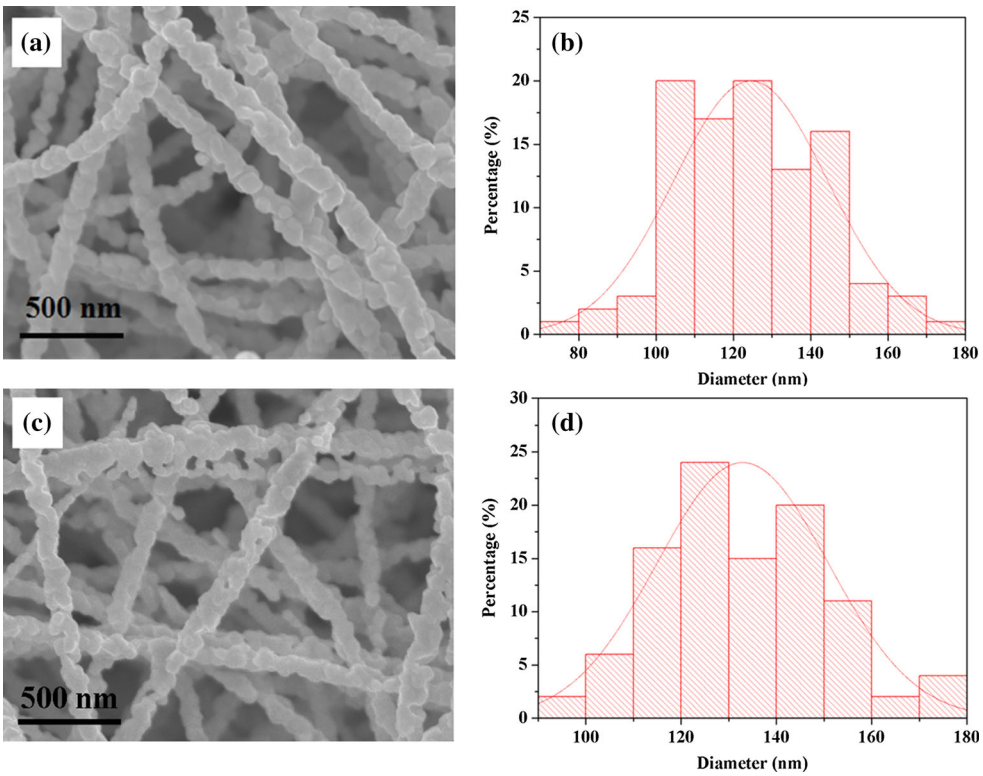

Fig. 3 SEM images (**a**, **c**) and histograms (**b**, **d**) of diameters of Bi_2MoO_6 (**a**, **b**) and Bi_2MoO_6/5 % RGO (**c**, **d**) composite nanofibers

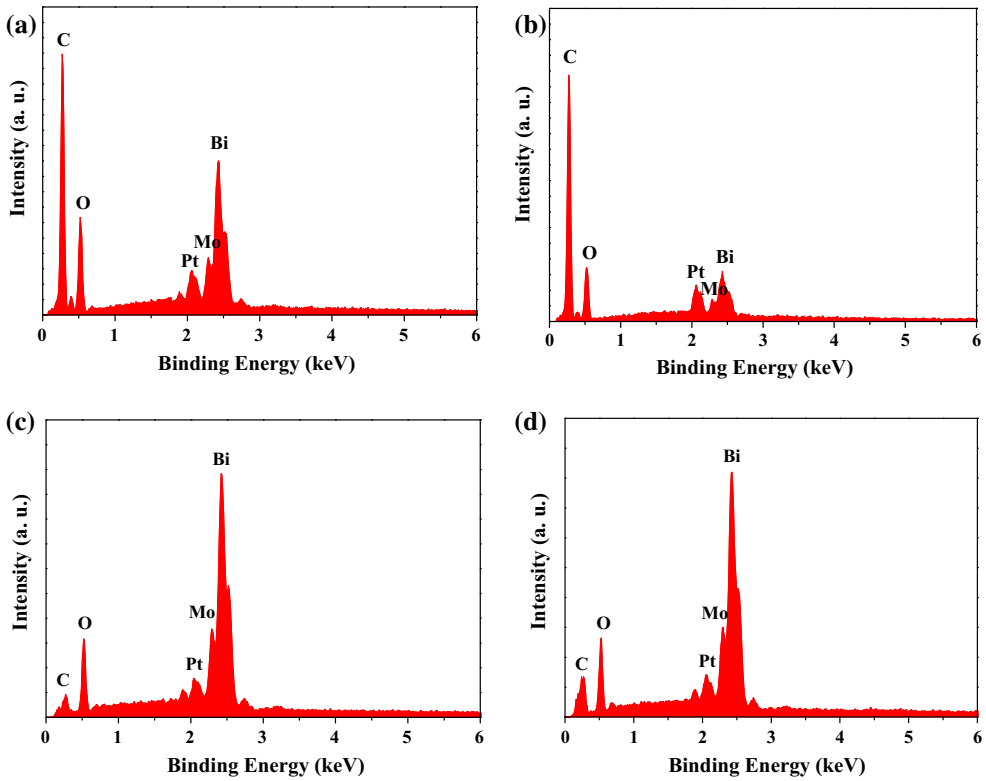

Fig. 4 EDX spectra of PVP/[$(NH_4)_6Mo_7O_{24}$ + $Bi(NO_3)_3$] (**a**), PVP/RGO/[$(NH_4)_6Mo_7O_{24}$ + $Bi(NO_3)_3$] (**b**), Bi_2MoO_6 (**c**) and Bi_2MoO_6/5 % RGO (**d**)

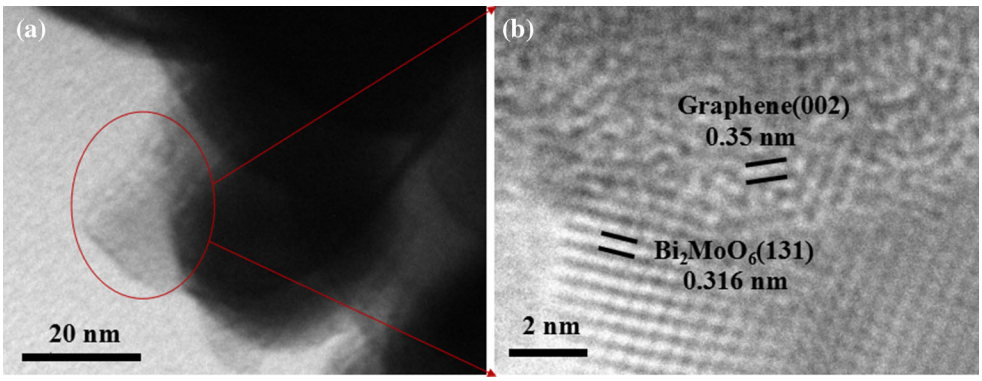

Fig. 5 TEM (**a**) and HRTEM (**b**) images of Bi_2MoO_6/5 % RGO composite nanofibers

3.3 Chemical bonds analysis

To further confirm the presence of RGO and the valence state of each element in the Bi_2MoO_6/5 % RGO composite nanofibers, the XPS spectra of Bi_2MoO_6 and Bi_2MoO_6/5 % RGO composites were recorded and shown in Fig. 6. As shown in Fig. 6a, the sample contains Bi, Mo, O and C elements. C in the Bi_2MoO_6 is ascribed to residual traces from the organics and the XPS instrument itself [35]. Figure 6b shows the high-resolution spectra of C 1s of the Bi_2MoO_6/5 % RGO composite nanofibers. Three peaks located at 284.7, 286.6 and 288.6 eV observed from the C 1s deconvolution spectrum of RGO correspond to the C–C, C–O and O–C=O (–COO–) groups, respectively [34]. The results indicate that the RGO is incorporated in the Bi_2MoO_6/5 % RGO composite nanofibers. As indicated in Fig. 6c, d, the peaks at 158.8 and 164.1 eV corresponding to Bi $4f_{7/2}$ and Bi $4f_{5/2}$ can be assigned to Bi^{3+} of Bi_2MoO_6/5 % RGO composites, and the peaks at 232.2 and 235.3 eV belong to Mo $3d_{5/2}$ and Mo $3d_{3/2}$, respectively, which are the features of Mo^{6+} in Bi_2MoO_6/5 % RGO [22]. Compared with Bi_2MoO_6, the peaks of Bi $4f_{7/2}$ and Bi $4f_{5/2}$ are shifted up by 0.2 eV, the peaks of Mo $3d_{5/2}$ and Mo $3d_{3/2}$ are shifted up by 0.2 eV. The higher peak binding

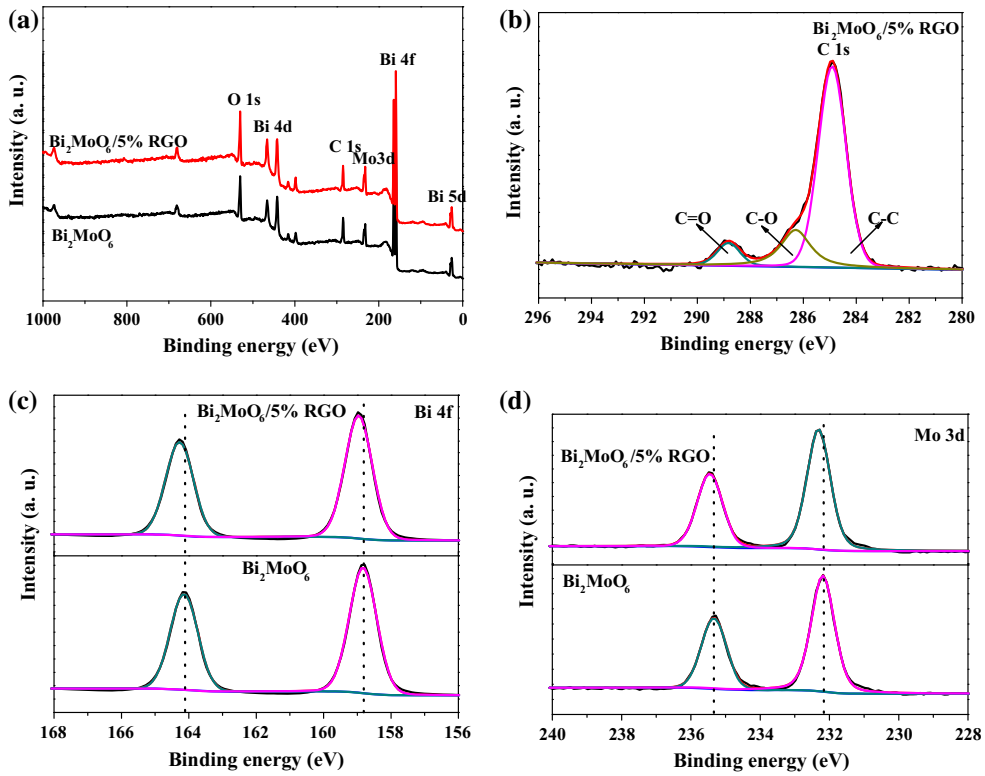

Fig. 6 XPS spectra of Bi_2MoO_6/5 % RGO and Bi_2MoO_6 ninofibers (**a**), C 1s of Bi_2MoO_6/5 % RGO (**b**), Bi 4f (**c**) and Mo 3d (**d**) of Bi_2MoO_6/5 % RGO and Bi_2MoO_6 ninofibers

energies for Bi 4f and Mo 3d of Bi_2MoO_6/5 % RGO are probably caused by electron transfer from surface groups of Bi_2MoO_6/5 % RGO to RGO sheets via the formed Bi(Mo)–O–C(RGO) bonds. Similar results have been already reported in Zn–Al LDH/CNTs and Bi_2MoO_6/Zn–Al heterostructures [21, 36].

3.4 UV–Vis absorption spectra

Figure 7 reveals the UV–Vis absorption spectra of Bi_2MoO_6 and Bi_2MoO_6/5 % RGO composites. Bi_2MoO_6 presents intense light absorption ranging from 200 to 480 nm and weak light absorption ranging from 480 to 800 nm. Bi_2MoO_6/5 % RGO exhibit similar absorption as that of Bi_2MoO_6, but the absorption intensity of Bi_2MoO_6/5 % RGO is higher than that of Bi_2MoO_6 in the region range from 200 to 800 nm. For crystalline semiconductors, the band gap energies of the samples can be estimated from a plot of $(\alpha hv)^{1/2}$ versus photon energy (hv). The indirect band gap energies of the samples are similar to the intercept of the tangent to the plot. The relationship between the absorption coefficient (α) and incident photon energy (hv) can be written as $\alpha = B_i(hv - Eg)^2/hv$, in which B_i is the absorption constant for indirect transitions [37]. As absorbance (A) is proportional to the absorption coefficient (α), here, α is substituted by A. Plots of $(Ahv)^{1/2}$ versus (hv) from the spectral data of Fig. 7 are presented in the insets of Fig. 7. The band gaps of Bi_2MoO_6 and Bi_2MoO_6/5 % RGO are 2.68 and 2.61 eV, respectively, indicating that RGO would almost unchange the band gap of Bi_2MoO_6 in the Bi_2MoO_6/5 % RGO composites. This result accords with that reported by Belver group [12].

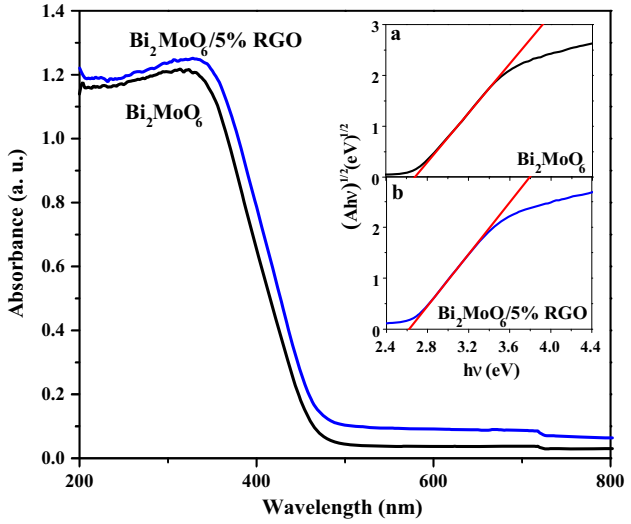

Fig. 7 UV–Vis absorption spectra of Bi_2MoO_6 and Bi_2MoO_6/5 % RGO composite nanofibers [*insets* present the corresponding plots of $(Ahv)^{1/2}$ vs photon energies (hv) of Bi_2MoO_6 (**a**) and Bi_2MoO_6/5 % RGO (**b**)]

3.5 Photocatalytic activity and mechanism

Figure 8 presents a comparison of the photocatalytic H_2-production activity of the samples Bi_2MoO_6, Bi_2MoO_6/xRGO (x = 2, 5, 8 %) and Bi_2MoO_6 + 5 % RGO composite nanofibers under 300 W Xe lamp irradiation using methanol as a scavenger. As can be seen from this figure, small amounts of hydrogen is detected when pure Bi_2MoO_6 is used as a photocatalyst. Methanol, which acts as a sacrificial electron donor, is able to rapidly remove the photo-generated holes and/or photo-generated oxygen in an irreversible fashion, thereby suppressing electron–hole recombination and/or the reverse reaction of H_2 and O_2 [38]. Therefore, even pure Bi_2MoO_6 could generate hydrogen in the aqueous solution under visible light irradiation. It is found that the content of RGO has a significant influence on the photocatalytic activity of Bi_2MoO_6. After introducing RGO, the activity of the Bi_2MoO_6/2 % RGO is slightly enhanced. The amount of hydrogen evolution is varied with the different amount of RGO by using Bi_2MoO_6/xRGO composites as photocatalyst. The photocatalytic activity of the samples further increases with increasing in RGO content from 2 to 5 %. The highest hydrogen evolution rate, obtained by using the Bi_2MoO_6/5 % RGO, is 794.72 μmol h^{-1}. This value is 2.86 times higher than that of Bi_2MoO_6 nanofibers. When RGO content is 8 %, higher than 5 %, the increase of RGO leads to a drastic reduction of the photocatalytic activity. This is probably due to high RGO load shielding the Bi_2MoO_6 from absorbing visible light [39]. Moreover, the excess RGO could absorb a certain amount of light and weaken the transmittance of incident light [40]. All these could decrease the photocatalytic performance of the photocatalyst, therefore, the amount of hydrogen produced is

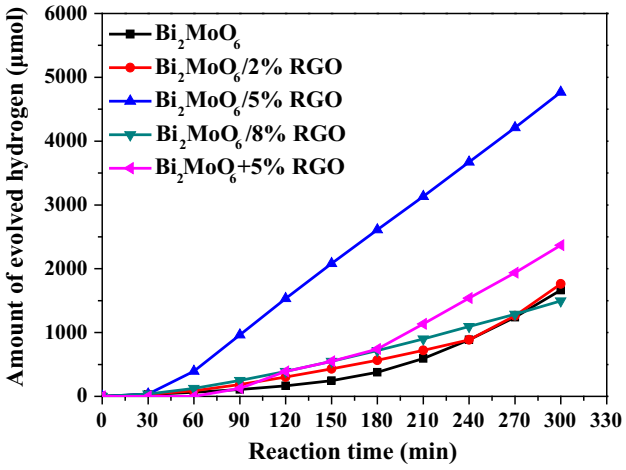

Fig. 8 Photocatalytic activities of Bi_2MoO_6, Bi_2MoO_6/2 % RGO, Bi_2MoO_6/5 % RGO, Bi_2MoO_6/8 % RGO and Bi_2MoO_6 + 5 % RGO composite nanofibers

decreased when RGO content is further increased. Specifically, the H_2-production activity of Bi_2MoO_6/5 % RGO prepared via electrospinning approach is greater than that of Bi_2MoO_6 + 5 % RGO (394.71 μmol h^{-1}) obtained by the simple mixing RGO nanosheets with solid Bi_2MoO_6 nanofibers. The results demonstrate definitely the preparation methods have an important effect on the photocatalytic performance of photocatalysts [41].

On the basis of the above discussion, a possible photocatalytic mechanism is proposed and displayed in Fig. 9. The CB potential of Bi_2MoO_6 was estimated based on the equation of $E_{CB} = X - E^c - 1/2E_g$, in which X is the electronegativity of Bi_2MoO_6, E^c is the energy of free electrons on the hydrogen scale (ca 4.5 eV), E_g is the band gap energy of the semiconductor. Based on the Mulliken electronegativity theory, the VB edge energy of Bi_2MoO_6 can be predicted by the equation of $E_{VB} = E_{CB} + E_g$. After calculation, it can be obtained that the positions of CB and VB edge potentials of Bi_2MoO_6 are determined to be 0.46 and 3.14 eV, respectively [42]. Under visible light irradiation, the electrons on the VB of Bi_2MoO_6 are excited to CB, creating holes (h^+) on the VB. Generally, these photogenerated electrons and holes quickly recombine and only portion of them participate in the photocatalytic reaction, reducing the photocatalytic activity of Bi_2MoO_6 [43]. However, when Bi_2MoO_6 is modified by RGO, these electrons on the CB of Bi_2MoO_6 tend to transfer to RGO sheets, improving the separation efficiency of charge carriers. It has been reported that the two-dimensional large π-conjugation structure of RGO facilitates the transfer of photoinduced electrons and can act as an excellent electron acceptor [44]. Because the potential of RGO/RGO^- (−0.08 eV vs. normal hydrogen electrode (NHE, pH = 0)) is more negative than the CB of Bi_2MoO_6 [45, 46], electron transfer occurs from RGO to Bi_2MoO_6 when they are in contact. The accumulation of electrons inevitably causes shifting of the apparent Fermi level. Thereby, the CB edge of RGO/Bi_2MoO_6 shifts negatively compared to that of Bi_2MoO_6. However, the *Eg* of RGO/Bi_2MoO_6 is nearly the same as that of Bi_2MoO_6. Thus, the electronic interaction between RGO and Bi_2MoO_6 might cause a cathodic shift of the CB edge, indicating higher CB position and a stronger reductive power which may be involved in the H_2O reduction reaction [47].

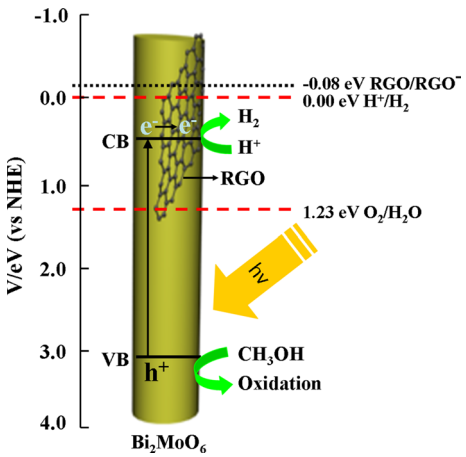

Fig. 9 Possible mechanism for photocatalytic H_2 evolution over Bi_2MoO_6/xRGO composite nanofibers under visible light irradiation

4 Conclusions

In summary, we have successfully fabricated Bi_2MoO_6/RGO composite nanofibers as photocatalyst for splitting water under visible light irradiation by calcining the electrospun PVP/RGO/[$(NH_4)_6Mo_7O_{24}$ + $Bi(NO_3)_3$] composite nanofibers. The as-prepared Bi_2MoO_6/RGO composite nanofibers with the diameter of 132 ± 18 nm have been demonstrated to be highly active photocatalysts for hydrogen evolution under visible light irradiation. Bi_2MoO_6/5 % RGO nanofibers exhibit the highest photocatalytic activity, and the H_2 evolution rate is observed to be as high as 794.72 μmol h^{-1}, 2.86 times than that of Bi_2MoO_6 nanofibers. These new findings imply that the performance of photocatalysts can be increased by the formation of Bi_2MoO_6/RGO nanocomposites. The enhanced photocatalytic activity could be attributed to the introduction of RGO and the nanofibrous morphology of the Bi_2MoO_6/RGO composite nanofibers obtained from electrospinning method. This work provides a new way toward the photocatalytic water splitting of Bi_2MoO_6 and demonstrates that RGO is a very promising candidate for development of high performance photocatalysts.

Acknowledgments This work was financially supported by the National Natural Science Foundation of China (51573023, 50972020, 51072026), Ph.D. Programs Foundation of the Ministry of Education of China (20102216110002, 20112216120003), the Science and Technology Development Planning Project of Jilin Province (Grant Nos. 20130101001JC, 20070402).

References

1. Y. Sung, J. Lim, J.H. Koh, L.J. Hill, B.K. Min, J. Pyun, K. Char, Uniform decoration of Pt nanoparticles on well-defined CdSe tetrapods and the effect of their Pt cluster size on photocatalytic H_2 generation. CrystEngComm **17**, 8423–8427 (2015)
2. T. Grewe, H. Tüysüz, Alkali metals incorporated ordered mesoporous tantalum oxide with enhanced photocatalytic activity for water splitting. J. Mater. Chem. A **4**, 3007–3017 (2016)
3. A. Fujishima, K. Honda, Electrochemical photolysis of water at a semiconductor electrode. Nature **238**, 37–38 (1972)
4. X.F. Zhou, Q.Z. Gao, X. Li, Y.J. Liu, S.S. Zhang, Y.P. Fang, J. Li, Ultra-thin SiC layers covered graphene nanosheets as dvanced

photocatalysts for hydrogen evolution. J. Mater. Chem. A **3**, 10999–11005 (2015)
5. M.Y. Wang, J. Ioccozia, L. Sun, C.J. Lin, Z.Q. Lin, Inorganic-modified semiconductor TiO_2 nanotube arrays for photocatalysis. Energy Environ. Sci. **7**, 2182–2202 (2014)
6. Y.H. Zhang, Y.J. Xu, Bi_2WO_6: a highly chemoselective visible light photocatalyst toward aerobic oxidation of benzylic alcohols in water. RSC Adv. **4**, 2904–2910 (2014)
7. D.J. Martin, K. Qiu, S.A. Shevlin, A.D. Handoko, X.W. Chen, Z.X. Guo, J.W. Tang, Highly efficient photocatalytic H_2 evolution from water using visible light and structure-controlled graphitic carbon nitride. Angew. Chem. Int. Ed. **53**, 9240–9245 (2014)
8. S.J. Hu, B. Chi, J. Pu, L. Jian, Surface charge modification in improvement of photocatalytic H_2 production over $La_2Ti_2O_7$/-graphene nanocomposite. RSC Adv. **4**, 60437–60444 (2014)
9. F.K. Ma, G. Zhao, C. Li, T.L. Wang, Y.Z. Wu, J.X. Lv, Y.Y. Zhong, X.P. Hao, Fabrication of CdS/BNNSs nanocomposites with broadband solar absorption for efficient photocatalytic hydrogen evolution. CrystEngComm **18**, 631–637 (2016)
10. M.Y. Zhang, C.L. Shao, J.B. Mu, X.M. Huang, Z.Y. Zhang, Z.C. Guo, P. Zhang, Y.C. Liu, Hierarchical heterostructures of Bi_2MoO_6 on carbon nanofibers: controllable solvothermal fabrication and enhanced visible photocatalytic properties. J. Mater. Chem. **22**, 577–584 (2012)
11. X. Wang, Fei Gu, L. Li, G. L. Fang, X. Wang. A facile mixed-solvothermal route to γ-Bi_2MoO_6 nanoflakes and their visible-light-responsive photocatalytic activity. Mater. Res. Bull. **48**, 3761–3765 (2013)
12. C. Belver, C. Adan, M.F. Garcia, Photocatalytic behaviour of Bi_2MoO_6 polymetalates for rhodamine B degradation. Catal. Today **143**, 274–281 (2009)
13. M.Y. Zhang, C.L. Shao, J.B. Mu, Z.Y. Zhang, Z.C. Guo, P. Zhang, Y.C. Liu, One-dimensional Bi_2MoO_6/TiO_2 hierarchical heterostructures with enhanced photocatalytic activity. CrystEngComm **14**, 605–612 (2012)
14. Y. Shimodaira, H. Kato, H. Kobayashi, A. Kudo, Photophysical properties and photocatalytic activities of bismuth molybdates under visible light irradiation. J. Phys. Chem. B **110**, 17790–17797 (2006)
15. Y.C. Miao, G.F. Pan, Y.N. Huo, H.X. Li, Aerosol-spraying preparation of Bi_2MoO_6: a visible photocatalyst in hollow microspheres with a porous outer shell and enhanced activity. Dyes Pigm. **99**, 382–389 (2013)
16. M.Y. Zhang, C.L. Shao, P. Zhang, C.Y. Su, X. Zhang, P.P. Liang, Y.Y. Sun, Y.H. Liu, Bi_2MoO_6 microtubes: controlled fabrication by using electrospun polyacrylonitrile microfibers as template and their enhanced visible light photocatalytic activity. J. Hazard. Mater. **225–226**, 155–163 (2012)
17. Y.S. Xu, W.D. Zhang, Monodispersed Ag_3PO_4 nanocrystals loaded on the surface of spherical Bi_2MoO_6 with enhanced photocatalytic performance. Dalton Trans. **42**, 1094–1101 (2013)
18. M. Shang, W.Z. Wang, J. Ren, S.M. Sun, L. Zhang, Nanoscale Kirkendall effect for the synthesis of Bi_2MoO_6 boxes via a facile solution-phase method. Nanoscale **3**, 1474–1476 (2011)
19. A. Martínez-de la Cruz, S. Obregón, Alfaro. Synthesis and characterization of γ-Bi_2MoO_6 prepared by co-precipitation: photoassisted degradation of organic dyes under vis-irradiation. J. Mol. Catal. A Chem. **320**, 85–91 (2010)
20. F. Zhou, R. Shi, Y.F. Zhu, Significant enhancement of the visible photocatalytic degradation performances of γ-Bi_2MoO_6 nanoplate by graphene hybridization. J. Mol. Catal. A Chem. **340**, 77–82 (2011)
21. H.P. Li, Q.H. Deng, J.Y. Liu, W.G. Hou, N. Du, R.J. Zhang, X.T. Tao, Synthesis, characterization and enhanced visible light photocatalytic activity of Bi_2MoO_6/Zn–Al layered double hydroxide hierarchical heterostructures. Catal. Sci. Technol. **4**, 1028–1037 (2014)
22. J. Di, J.X. Xia, M.X. Ji, H.P. Li, H. Xu, H.M. Li, R. Chen, The synergistic role of carbon quantum dots for the improved photocatalytic performances of Bi_2MoO_6. Nanoscale **7**, 11433–11443 (2015)
23. D. Chen, L. Tang, J. Li, Graphene-based materials in electrochemistry. Chem. Soc. Rev. **39**, 3157–3180 (2010)
24. Q. Xiang, J.G. Yu, M. Jaroniec, Graphene-based semiconductor photocatalysts. Chem. Soc. Rev. **41**, 782–796 (2012)
25. Y. Zhang, Y.K. Zhu, J.Q. Yu, D.J. Yang, T.W. Ng, P.K. Wong, J.C. Yu, Enhanced photocatalytic water disinfection properties of Bi_2MoO_6–RGO nanocomposites under visible light irradiation. Nanoscale **5**, 6307–6310 (2013)
26. P.F. Wang, Y.H. Ao, C. Wang, J. Hou, J. Qian, A one-pot method for the preparation of graphene-Bi_2MoO_6 hybrid photocatalysts that are responsive to visible-light and have excellent photocatalytic activity in the degradation of organic pollutants. Carbon **50**, 5256–5264 (2012)
27. X.J. Zhou, Q.L. Ma, W.S. Yu, T.T. Wang, X.T. Dong, J.X. Wang, G.X. Liu, Magnetism and white-light-emission bifunctionality simultaneously assembled into flexible janus nanofiber via electrospinning. J. Mater. Sci. **50**, 7884–7895 (2015)
28. K. Lun, Q.L. Ma, M. Yang, X.T. Dong, Y. Yang, J.X. Wang, W.S. Yu, G.X. Liu, Color-tunable luminescence nanofibers endowed with simultaneously tuned electricity–magnetism performance. J. Mater. Sci.: Mater. Electron. **26**, 5994–6003 (2015)
29. L. Han, M.M. Pan, Y. Lv, Y.T. Gu, X.F. Wang, D. Li, Q.L. Kong, X.T. Dong, Fabrication of Y_2O_2S:Eu^{3+} hollow nanofibers by sulfurization of Y_2O_3:Eu^{3+} hollow nanofibers. J. Mater. Sci.: Mater. Electron. **26**, 677–684 (2015)
30. J. Tian, Q.L. Ma, X.T. Dong, M. Yang, Y. Yang, J.X. Wang, W.S. Yu, G.X. Liu, Flexible composite nanobelts: facile electrospinning construction, structure and color-tunable photoluminescence. J. Mater. Sci.: Mater. Electron. **26**, 8413–8420 (2015)
31. K.S. Divya, T.U. Umadevi, S. Mathew, Graphene-based semiconductor nanocomposites for photocatalytic applications. J. Nanosci. Lett. **4**, 21 (2014)
32. C. Hou, Q. Zhang, M. Zhu, Y. Li, H. Wang, One-step synthesis of magnetically-functionalized reduced graphite sheets and their use in hydrogels. Carbon **49**, 47–53 (2011)
33. Y. Ma, Y.L. Jia, Z.B. Jiao, M. Yang, Y.X. Qi, Y.P. Bi, Hierarchical Bi_2MoO_6 nanosheet-built frameworks with excellent photocatalytic properties. Chem. Commun. **51**, 6655–6658 (2015)
34. C.Y. He, R.H. Wang, H.G. Fu, P.K. Shen, Nitrogen-self-doped graphene as a high capacity anode material for lithium-ion batteries. J. Mater. Chem. A **1**, 14586–14591 (2013)
35. W. Geng, X.F. Zhao, W.Y. Zan, H.X. Liu, X.J. Yao, Effects of the electric field on the properties of ZnO–graphene composites: a density functional theory study. Phys. Chem. Chem. Phys. **16**, 3542–3548 (2014)
36. Z. Zhang, C. Shao, X. Li, Y. Sun, M. Zhang, J. Mu, P. Zhang, Z. Guo, Y. Liu, Hierarchical assembly of ultrathin hexagonal SnS_2 nanosheets onto electrospun TiO_2 nanofibers: enhanced photocatalytic activity based on photoinduced interfacial charge transfer. Nanoscale **5**, 606–618 (2013)
37. C.H. Wang, C.L. Shao, Y.C. Liu, X.H. Li, Water-dichloromethane interface controlled synthesis of hierarchical rutile TiO_2 superstructures and their photocatalytic properties. Inorg. Chem. **48**, 1105–1113 (2009)
38. R.P. Panmand, Y.A. Sethi, S.R. Kadam, M.S. Tamboli, L.K. Nikam, J.D. Ambekar, C.-J. Park, B.B. Kale, Self-assembled hierarchical nanostructures of Bi_2WO_6 for hydrogen production and dye degradation under solar light. CrystEngComm **17**, 107–115 (2015)

39. S.J. Hu, B. Chi, J. Pu, L. Jian, Surface charge modification for improvement of photocatalytic H_2 production over a $La_2Ti_2O_7$/-graphene nanocomposite. RSC Adv. **4**, 60437–60444 (2014)
40. M. Orlita, C. Faugeras, P. Plochocka, P. Neugebauer, G. Martinez, D.K. Maude, A.L. Barra, M. Sprinkle, C. Berger, W.A. de Heer, M. Potemski, Approaching the dirac point in high-mobility multilayer epitaxial graphene. Phys. Rev. Lett. **101**, 267601 (2008)
41. J. Yang, X.H. Wang, X.L. Zhao, J. Dai, S.R. Mo, Synthesis of uniform Bi_2WO_6-reduced graphene oxide nanocomposites with significantly enhanced photocatalytic reduction activity. J. Phys. Chem. C **119**, 3068–3078 (2015)
42. X. Lin, X.Y. Guo, Q.W. Wang, L.M. Chang, H.J. Zhai, Hydrothermal synthesis and efficient visible light photocatalytic activity of Bi_2MoO_6/$BiVO_4$ heterojunction. Acta Phys. Chim. Sin. **30**, 2113–2120 (2014)
43. J.G. Yu, W.G. Wang, B. Cheng, B.L. Su, Enhancement of photocatalytic activity of mesporous TiO_2 powders by hydrothermal surface fluorination treatment. J. Phys. Chem. C **113**, 6743–6750 (2009)
44. H. Zhang, X.J. Lv, Y.M. Li, Y. Wang, J.H. Li, P_{25}-graphene composite as a high performance photocatalyst. ACS Nano **4**, 380–386 (2010)
45. K.F. Zhou, Y.H. Zhu, X.L. Yang, X. Jiang, C.Z. Li, Preparation of graphene–TiO_2 composites with enhanced photocatalytic activity. New J. Chem. **35**, 353–359 (2011)
46. J.G. Yu, J.R. Ran, Facile preparation and enhanced photocatalytic H_2-production activity of $Cu(OH)_2$ cluster modified TiO_2. Energy Environ. Sci. **4**, 1364–1371 (2011)
47. E.P. Gao, W.Z. Wang, M. Shang, J.H. Xu, Synthesis and enhanced photocatalytic performance of graphene–Bi_2WO_6 composite. Phys. Chem. Chem. Phys. **13**, 2887–2893 (2011)